AGU PUBLICATIONS

JGR

Journal of Geophysical Research: Space Physics

RESEARCH ARTICLE

10.1002/2015JA022042

Key Points:
- Alfven-cyclotron and ion Bernstein instabilities driven by a proton velocity ring distribution
- Despite their smaller linear growth rates, the Alfven-cyclotron modes saturate at a larger level
- Bernstein and Alfven-cyclotron modes, respectively, lead to perpendicular and pitch angle scattering

Correspondence to:
K. Min,
kmin@auburn.edu

Citation:
Min, K., and K. Liu (2016), Proton velocity ring-driven instabilities in the inner magnetosphere: Linear theory and particle-in-cell simulations, *J. Geophys. Res. Space Physics*, *121*, 475–491, doi:10.1002/2015JA022042.

Received 15 OCT 2015
Accepted 4 JAN 2016
Accepted article online 25 JAN 2016
Published online 30 JAN 2016

Proton velocity ring-driven instabilities in the inner magnetosphere: Linear theory and particle-in-cell simulations

Kyungguk Min[1] and Kaijun Liu[1]

[1]Department of Physics, Auburn University, Auburn, Alabama, USA

Abstract Linear dispersion theory and electromagnetic particle-in-cell (PIC) simulations are used to investigate linear growth and nonlinear saturation of the proton velocity ring-driven instabilities, namely, ion Bernstein instability and Alfvén-cyclotron instability, which lead to fast magnetosonic waves and electromagnetic ion cyclotron waves in the inner magnetosphere, respectively. The proton velocity distribution is assumed to consist of 10% of a ring distribution and 90% of a low-temperature Maxwellian background. Here two cases with ring speeds $v_r/v_A = 1$ and 2 (v_A is the Alfvén speed) are examined in detail. For the two cases, linear theory predicts that the maximum growth rate γ_m of the Bernstein instability is $0.16\Omega_p$ and $0.19\Omega_p$, respectively, and γ_m of the Alfvén-cyclotron instability is $0.045\Omega_p$ and $0.15\Omega_p$, respectively, where Ω_p is the proton cyclotron frequency. Two-dimensional PIC simulations are carried out for the two cases to examine the instability development and the corresponding evolution of the particle distributions. Initially, Bernstein waves develop and saturate with strong electrostatic fluctuations. Subsequently, electromagnetic Alfvén-cyclotron waves grow and saturate. Despite their smaller growth rate, the saturation levels of the Alfvén-cyclotron waves for both cases are larger than those of the Bernstein waves. Resonant interactions with the Bernstein waves lead to scattering of ring protons predominantly along the perpendicular velocity component (toward both decreasing and, at a lesser extent, increasing speeds) without substantial change of either the parallel temperature or the temperature anisotropy. Consequently, the Alfvén-cyclotron instability can still grow. Furthermore, the free energy resulting from the pitch angle scattering by the Alfvén-cyclotron waves is larger than the free energy resulting from the perpendicular energy scattering, thereby leading to the larger saturation level of the Alfvén-cyclotron waves.

1. Introduction

Proton ring-like velocity distributions or, more generally, proton velocity distributions with $\partial f_p(v_\perp)/\partial v_\perp > 0$ are frequently observed in the inner magnetosphere [*Meredith et al.*, 2008; *Chen et al.*, 2011; *Thomsen et al.*, 2011; *Ma et al.*, 2014; *Balikhin et al.*, 2015], and have been obtained from the magnetospheric ring current model [e.g., *Jordanova et al.*, 1997]. *Chen et al.* [2010a, 2010b] used the ring current ion distributions obtained from such a model to show that two distinct types of potentially unstable proton velocity distributions can arise. The proton distributions near midnight are essentially bi-Maxwellian with $T_\perp/T_\parallel > 1$ as a result of fresh ion injection from the nightside, where T is the temperature and the subscripts denote directions relative to the background magnetic field $\mathbf{B}_0$. However, the energy-dependent ion drift leads to ring-like velocity distributions between prenoon and duskside [*Chen et al.*, 2010b, Figure 4]; protons above 10 keV drift westward due to the dominant $\nabla\mathbf{B}$ drift, while protons below 1 keV are predominately subject to the $\mathbf{E}\times\mathbf{B}$ drift in the eastward direction. At the same time, $T_\perp/T_\parallel$ increases and reaches its maximum near prenoon at $L \sim 4.5$. The ring speed v_r is greater than $2v_A$ in the plasmasphere near the duskside, where v_A is the Alfvén speed, and falls down to $\sim v_A$ beyond noon where the electron density becomes low. Observationally, *Meredith et al.* [2008] showed that proton rings with the ring speed exceeding the Alfvén speed occur on the duskside, both inside and outside the plasmapause, where fast magnetosonic waves were simultaneously observed. *Thomsen et al.* [2011] showed that the peak occurrence of positive slopes of ion distributions is between midmorning and dusk and moves progressively toward earlier local times for higher energies.

For conditions of the inner magnetosphere, two classes of electromagnetic waves that can be driven by such ring-like proton velocity distributions with sufficient temperature anisotropy are frequently observed near the geomagnetic equator with frequencies on the order of the proton cyclotron frequency Ω_p. One class is

electromagnetic ion cyclotron (EMIC) waves driven by the temperature anisotropy of energetic ring current ions with energies of tens of keV [e.g., *Cornwall*, 1965; *Kennel and Petschek*, 1966; *Gary et al.*, 1994, 2012]. The presence of heavy ions, namely, helium and oxygen ions, complicates the overall picture of the instability by introducing cyclotron damping at the corresponding cyclotron frequencies and two stop bands below Ω_p, resulting in three distinct bands of EMIC waves [*Gomberoff and Neira*, 1983; *Kozyra et al.*, 1984]. While the ion composition, the electron plasma-to-cyclotron frequency ratio ω_{pe}/Ω_e, and $T_\parallel$ and $T_\perp/T_\parallel$ of the energetic ions determine the growth rate and the frequency band of the most unstable mode [*Gendrin et al.*, 1984; *Horne and Thorne*, 1994; *Gary et al.*, 2012; *Lee and Angelopoulos*, 2014; *Denton et al.*, 2015], the maximum growing modes generally have wave numbers at $k\lambda_p \leq 1$, propagate parallel to $\mathbf{B}_0$ with left-hand polarization, and are highly electromagnetic ($|\delta\mathbf{E}|^2/|\delta\mathbf{B}|^2 < 1$), where λ_p is the proton inertial length and $\delta\mathbf{E}$ and $\delta\mathbf{B}$ are, respectively, electric and magnetic field fluctuations. Much of local excitation and subsequent propagation away from the source region for EMIC waves has been understood through theory and modeling [*Gary et al.*, 1994; *Horne and Thorne*, 1994; *Jordanova et al.*, 2001; *Khazanov et al.*, 2006; *Gamayunov and Khazanov*, 2008; *Chen et al.*, 2010a; *Hu et al.*, 2010; *Omidi et al.*, 2010; *Denton et al.*, 2014], and observations [*Loto'aniu et al.*, 2005; *Blum et al.*, 2009, 2012; *Zhang et al.*, 2014; *Min et al.*, 2015]. In recent years, EMIC waves are thought to play an important role in radiation belt electron loss through pitch angle scattering [*Meredith et al.*, 2003; *Shprits et al.*, 2008; *Millan and Thorne*, 2007; *Xiao et al.*, 2011; *Shprits et al.*, 2013; *Usanova et al.*, 2014; *Kersten et al.*, 2014; *Ma et al.*, 2015].

Another class is fast magnetosonic waves which have $|\delta B_\parallel|^2 > |\delta B_\perp|^2$, propagate quasi-perpendicular to $\mathbf{B}_0$ ($0 < k_\parallel \ll k_\perp$), and are confined to within $\sim 2°$ of the magnetic equatorial plane [*Russell et al.*, 1970; *Gurnett*, 1976; *Laakso et al.*, 1990; *Kasahara et al.*, 1994; *Santolík et al.*, 2004; *Němec et al.*, 2005, 2006; *Hrbáčková et al.*, 2015]. A defining signature of these waves is a series of discrete, narrow tones at multiples of Ω_p present in the frequency spectrum between $\sim \Omega_p$ up to and beyond the lower hybrid frequency ω_{lh}, although in some cases the harmonic spacings can vary [*Gurnett*, 1976; *Santolík et al.*, 2002; *Posch et al.*, 2015] perhaps related to radial propagation from the distant source region [*Perraut et al.*, 1982; *Xiao et al.*, 2012, 2015a]. Such wave properties, especially the proton cyclotron harmonic dispersion, are consistent with those of the growing modes driven by the proton ring-like velocity distributions [*Gul'elmi et al.*, 1975; *Curtis and Wu*, 1979; *Perraut et al.*, 1982; *McClements and Dendy*, 1993; *McClements et al.*, 1994; *Horne et al.*, 2000; *Chen et al.*, 2010b; *Denton et al.*, 2010; *Gary et al.*, 2010, 2011a; *Liu et al.*, 2011a; *Min and Liu*, 2015a; *Chen*, 2015], which were often observed together with the waves [*Perraut et al.*, 1982; *Boardsen et al.*, 1992; *Meredith et al.*, 2008; *Xiao et al.*, 2013; *Ma et al.*, 2014; *Zhou et al.*, 2014; *Posch et al.*, 2015]. Given these properties, *Gary et al.* [2010, 2011a] suggests that the associated instability should be referred to as ion Bernstein instability. Fast magnetosonic waves can accelerate and pitch angle scatter radiation belt electrons through resonant and nonresonant interactions [*Horne et al.*, 2007; *Bortnik and Thorne*, 2010; *Chen et al.*, 2015; *Xiao et al.*, 2015b].

An important, but overlooked aspect of the proton ring-like velocity distributions in the inner magnetosphere is that for a sufficiently large ring speed and/or sufficiently small $T_\parallel$, they can be very anisotropic and thus should be unstable to the growth of the temperature-anisotropy-driven waves, such as EMIC waves, in addition to the fast magnetosonic waves due to $\partial f_p(v_\perp)/\partial v_\perp > 0$ [e.g., *Mithaiwala et al.*, 2013; *Vandas and Hellinger*, 2015]. However, considering prevalence of the ring-like velocity distributions as the models and observations above have shown, previous studies have only investigated either ion Bernstein or Alfvén-cyclotron instabilities and, to our knowledge, there have been no studies reporting the simultaneous development of the two instabilities, their interaction, and the implication on magnetospheric wave and particle dynamics. This study focuses on the simultaneous development of the two instabilities driven by a proton ring velocity distribution.

The goal here is threefold. First, we will provide a comprehensive picture of both instabilities across all wave normal angles, using fully kinetic dispersion theory for the ring velocity distributions [*Umeda et al.*, 2012; *Min and Liu*, 2015a]. For systematic analyses, we will assume a simplified two-component proton velocity distribution, $f_p = f_r + f_M$, where f_M represents Maxwellian background protons with a small temperature, and f_r represents a nondrifting ring (equation (1)) of energetic protons. Helium and oxygen ions are excluded in the current study for simplicity. Second, we will carry out two-dimensional particle-in-cell (PIC) simulations to examine the instability development and to investigate nonlinear saturation of the Alfvén-cyclotron and Bernstein modes. Last, we will examine how two types of instabilities compete for free energy and affect the evolution of f_p. The paper is organized as follows. Section 2 describes the proton velocity distribution model

and the linear dispersion relation solver used as well as the setup of the PIC simulations performed. Results of linear theory and PIC simulations are presented in section 3. Sections 4 and 5 are devoted to discussions and summary of the results, respectively.

Throughout the paper, we denote the jth species plasma frequency as $\omega_{pj} \equiv \sqrt{4\pi n_j e^2/m_j}$, the jth species cyclotron frequency as $\Omega_j \equiv e_j B_0/m_j c$, and the jth component beta as $\beta_j \equiv 8\pi n_j T_j/B_0^2$. Additionally, we define $\tilde{\beta}_j \equiv 8\pi n_0 T_j/B_0^2$ following *Gary et al.* [2010]. The Alfvén speed is $v_A \equiv B_0/\sqrt{4\pi n_0 m_p}$, the proton inertial length is $\lambda_p \equiv \sqrt{m_p c^2/4\pi n_0 e^2}$, and the lower hybrid frequency is $\omega_{lh} = \omega_{pp}/\sqrt{1+\omega_{pe}^2/\Omega_e^2}$. Here n_0 is equal to the unperturbed electron density n_e.

Carrying out fully kinetic, fully electromagnetic two-dimensional PIC simulations to resolve the two instabilities that have different spatiotemporal scales is computationally challenging. Given our limited computational resources, we here resort to a reduced system which is, nevertheless, sufficient for understanding essential physics. Consistent with the previous studies [*Liu et al.*, 2011a; *Min and Liu*, 2015a, 2015b], a reduced proton-to-electron mass ratio of $m_p/m_e = 100$ and a relatively small light-to-Alfvén speed ratio of $c/v_A = 15$ (equivalently $\omega_{pe}/\Omega_e = 1.5$) are assumed. The reduced parameters result in $\omega_{lh} \approx 8.3\Omega_p$ and allow a reasonably large simulation time step without violating stability conditions of PIC simulations.

The proton distribution model used is certainly different from the conditions in the inner magnetosphere. For example, energetic particles of the magnetospheric plasma often have a high-energy tail so a kappa-type distribution may be a better choice [*Viñas et al.*, 2005; *Xiao et al.*, 2007, 2008]. And the effect of heavy ions not included can modify the dispersion characteristics of EMIC waves by introducing the two stop bands. Furthermore, the reduced parameters chosen for simulations are certainly unrealistic. Therefore, this study does not intend to reproduce the observed wave phenomena. However, the proton model chosen can still provide invaluable insights into the relevant instabilities and the simulations based on the reduced parameters still preserve the essential physics of wave-particle interactions, the understanding of which is the main focus of this study.

2. Methodology

To represent the velocity ring condition of $\partial f_p(v_\perp)/\partial v_\perp > 0$ at suprathermal proton speeds, we here consider the proton velocity distribution constructed from two components in the form $f_p(\mathbf{v}) = f_r(v_\parallel, v_\perp) + f_M(v_\parallel, v_\perp)$, where each component can be represented by a nondrifting ring velocity distribution

$$f_j(v_\parallel, v_\perp) = \frac{n_j}{\pi^{3/2}\theta_j^3 A_j} e^{-v_\parallel^2/\theta_j^2} e^{-(v_\perp - v_j)^2/\theta_j^2}, \tag{1}$$

where $A_j = \exp(-v_j^2/\theta_j^2) + \sqrt{\pi}(v_j/\theta_j)\,\mathrm{erfc}(-v_j/\theta_j)$ is jth component's normalization constant and v_j and θ_j are jth component's ring speed and thermal spread of the ring, respectively. Here f_M is the thermal proton background with a Maxwellian distribution (i.e., $v_M = 0$) with $\tilde{\beta}_M = \theta_M^2/v_A^2 = 0.002$ (using the definitions in section 1). The other component, f_r, is the ring velocity distribution (i.e., $v_r > 0$) with $\theta_r^2/v_A^2 = 0.2$. Additionally, electrons are represented by a single Maxwellian velocity distribution with $\beta_e = \tilde{\beta}_M$. These base parameters are consistent with those of *Liu et al.* [2011a] and *Min and Liu* [2015a, 2015b], so the results here can be directly compared to theirs. Since it has been shown that the ring speed in the inner magnetosphere associated with fast magnetosonic waves can vary from below v_A to above $2v_A$ [*Horne et al.*, 2000; *Meredith et al.*, 2008; *Chen et al.*, 2010b; *Thomsen et al.*, 2011; *Ma et al.*, 2014], we accordingly choose two representative cases, $v_r/v_A = 1$ and 2. Later, we vary the ring concentration n_r/n_e to investigate the linear instability scaling on n_r/n_e. Table 1 lists five sets of ring proton parameters to be used in the study. The table also includes effective temperature anisotropies ($T_{\perp r}/T_{\parallel r}$) of f_r, the ratio of the perpendicular to parallel second velocity moments, $\langle v_\perp^2\rangle/\langle 2v_\parallel^2\rangle$ (for $v_r/\theta_r \gg 1$, $T_{\perp r}/T_{\parallel r} \approx 3/2 + v_r^2/\theta_r^2$). With $\tilde{\beta}_{\parallel r}$, this is an important parameter to determine the properties of the Alfvén-cyclotron instability [e.g., *Kennel and Petschek*, 1966; *Gary et al.*, 2012].

For linear theory analyses, the dispersion solver developed by *Min and Liu* [2015a] is used to solve the fully kinetic dispersion equation corresponding to the two-component proton model for the complex frequency $\omega = \omega_r + i\gamma$ at given pairs of the wave normal angle ψ ranging from 0° to 90° in steps of 1° for $\psi \gtrsim 45°$ and 5° for $\psi \lesssim 45°$, and the wave number $k \lesssim 100\lambda_p^{-1}$ with varying step sizes. The dispersion solver directly accepts velocity distributions constructed from multiple rings of equation (1) and is therefore appropriate for the current analyses.

Table 1. Parameters of Two-Component Proton Model and Maximum Linear Instabilities[a]

Model	n_r/n_e	v_r/v_A	$T_\perp/T_\parallel$	ω_m^{IB}/Ω_p	$k_m^{IB}\lambda_p$	ψ_m^{IB}	ω_m^{AC}/Ω_p	$k_m^{AC}\lambda_p$
1	0.1	2.0	21.3	$9.7+0.19i$	7.06	74°	$0.63+0.15i$	0.95
2	0.1	1.0	6.44	$6+0.16i$	10.1	90°	$0.6+0.045i$	0.89
3	0.01	2.0	21.3	$3+0.049i$	3.2	90°	$0.59+0.023i$	0.9
4	0.5	1.0	6.44	$3.96+0.33i$	8.48	90°	$0.65+0.15i$	0.94
5	0.5	2.0	21.3	$15.6+0.68i$	11.4	72°	$0.82+0.47i$	1.25

[a]Superscripts IB and AC denote ion Bernstein and Alfvén-cyclotron instabilities, respectively, and subscript *m* means value of the quantity at the maximum growth rate.

For two-dimensional kinetic simulations, we adopt the PIC code developed by *Liu* [2007]. The code self-consistently solves a coupled system of nonrelativistic equations of charged particles' motion and Maxwell's equations, using the second-order accurate, centered-difference scheme for spatial derivatives, the Boris scheme for particle acceleration, and the explicit leapfrog scheme for temporal integration [*Birdsall and Langdon*, 1985]. This code has since been used for many studies including banded chorus [*Liu et al.*, 2011b; *Gary et al.*, 2011b; *Fu et al.*, 2014] and fast magnetosonic waves [*Liu et al.*, 2011a; *Min and Liu*, 2015a].

Here we carry out two simulation runs corresponding to models 1 and 2, for which the maximum growth rate γ_m is sufficiently large for all of the wave modes of interest to grow to a sufficient level within reasonable computation times. The simulation domain is contained in the *x*-*y* plane with the uniform background magnetic field $\mathbf{B}_0$ along the *x* direction. Periodic boundary conditions are used in both dimensions, so the results to be presented in the following sections are appropriate within the small region of the geomagnetic equator where the waves grow locally. We choose the simulation sizes $L_x = 120\lambda_p$ and $L_y = 48\lambda_p$, and the number of

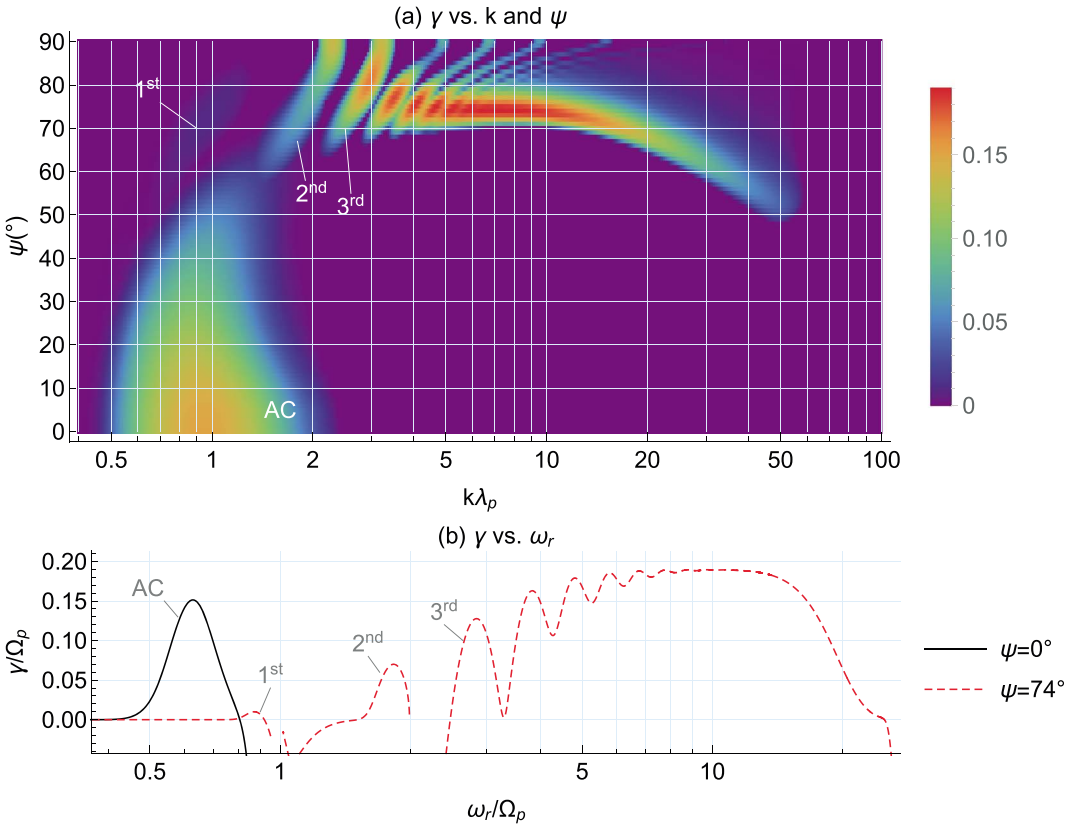

Figure 1. Linear theory results for model 1. (a) Growth rate ($\gamma > 0$) normalized to Ω_p of the AC and IB instabilities as a function of $\psi(°)$ and $k\lambda_p$. (b) Line plots of γ/Ω_p at $\psi = 0°$ (solid) and $\psi = 74°$ (dashed) as a function of ω_r/Ω_p. Label "AC" denotes the region of the unstable AC mode, and labels "1st," "2nd," and "3rd" denote the fundamental, second, and third harmonics of the unstable IB modes.

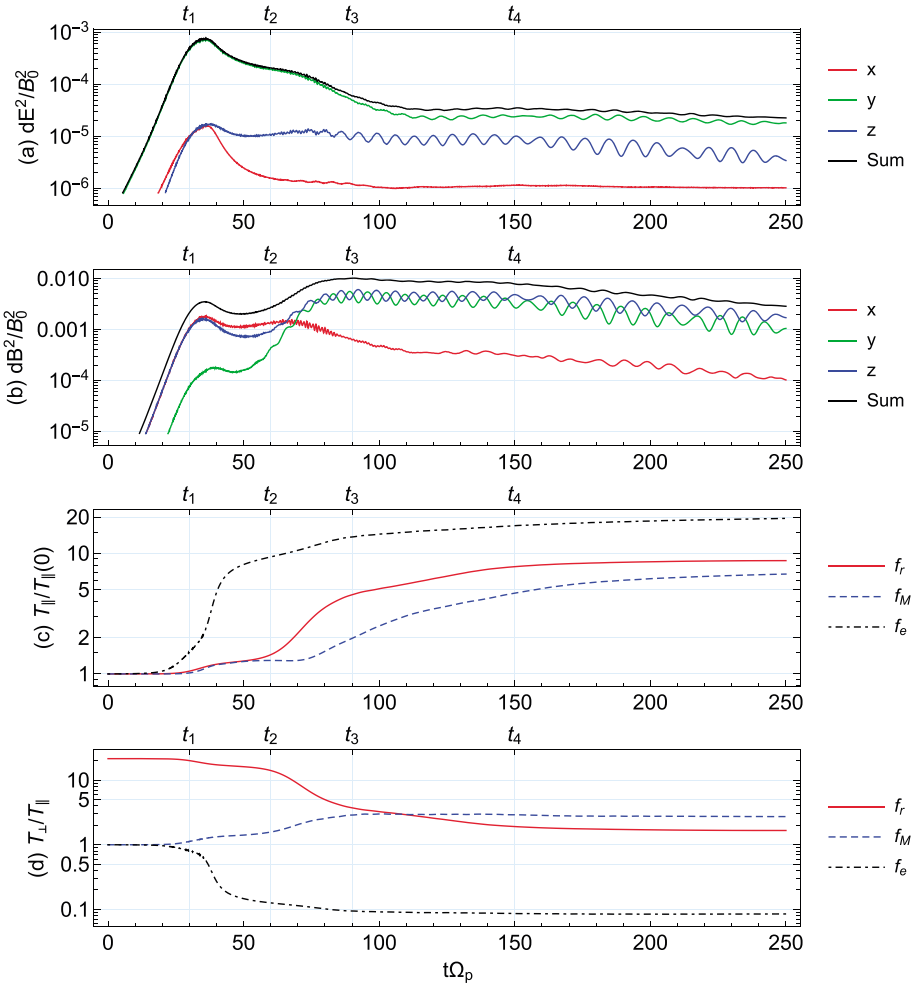

Figure 2. Time evolution of the simulated field energies and particle temperatures for model 1. Shown from the top are (a) electric and (b) magnetic field energies, (c) parallel temperatures of components/species, and (d) temperature anisotropy of components/species. Four selected times $t_1 - t_4$ marked are at $30\Omega_p^{-1}$, $60\Omega_p^{-1}$, $90\Omega_p^{-1}$, and $150\Omega_p^{-1}$, respectively.

cells $N_x = N_y = 960$. Such a domain setup allows us to simultaneously resolve both the ion Bernstein modes of large wave number at the quasi-perpendicular direction and the Alfvén-cyclotron modes of small wave number at the parallel direction. The reduced parameters, $m_p/m_e = 100$ and $c/v_A = 15$, enable a reasonably large time step $\Delta t = 0.001\Omega_p^{-1}$. We use 2500 simulation particles per cell per component in the simulations.

3. Results

This section describes linear theory and PIC simulation results from models with two different values of the ring speed. As stated in Table 1, model 1 corresponds to $v_r/v_A = 2$, whereas model 2 corresponds to $v_r/v_A = 1$; all other dimensionless parameters are the same for the two cases.

3.1. Large Ring Speed (Model 1)

Figure 1a displays the linear growth rate (only for $\gamma > 0$) for proton model 1 as functions of k and ψ. To produce this figure, we have chosen the maximum growth rate among all solutions at given k and ψ, as the ion Bernstein modes have multiple dispersion surfaces at different frequencies. The Alfvén-cyclotron (AC) modes are unstable at $\psi \lesssim 60°$ and wave numbers ranging $0.5\lambda_p^{-1} \lesssim k \lesssim 2\lambda_p^{-1}$, but the maximum growth rate appears at $\psi = 0°$ and $k \approx 0.95\lambda_p^{-1}$. The ion Bernstein (IB) modes, in contrast, exhibit a rather complex structure. Above roughly $\psi = 88°$, all the harmonic modes are discrete in wave number space (and in frequency space as well). As ψ decreases, the discrete harmonic dispersion becomes continuous starting from the high harmonic modes, also shown in *Horne et al.* [2000]. Exceptions are the fundamental and second harmonic

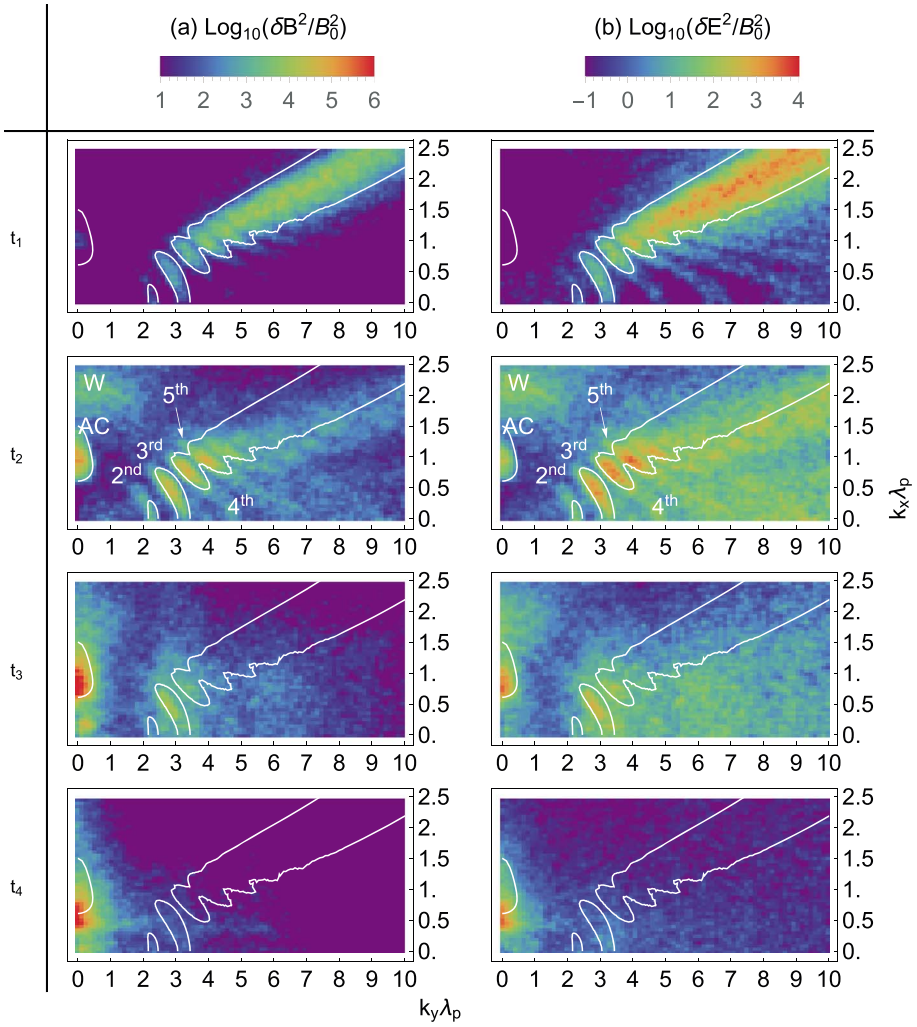

Figure 3. Four snapshots of the simulated wave power spectra corresponding to $t_1 - t_4$ for model 1. The (left column) magnetic and (right column) electric wave power spectra are shown as a function of $k_x\lambda_p$ (vertical axis) and $k_y\lambda_p$ (horizontal axis). The white contours delineate the linear growth rate of $\gamma = 0.1\Omega_p$. Labels AC, 2nd, 3rd, 4th, and 5th denote the AC mode and second-to-fifth harmonics of the IB modes, respectively. Label "W" denotes the nonphysical whistler mode discussed in the text.

modes (labeled as 1st and 2nd in the figure, respectively). All harmonic modes are basically unstable, but the fundamental mode with $\gamma > 0$ does not appear until $\psi \leq 83°$ and is only marginally unstable. All IB modes are damped below $\psi \approx 50°$. Despite the large anisotropy of the ring protons ($T_{\perp r}/T_{\parallel r} \approx 21.3$), the IB mode located at $k_m^{IB} = 7.06\lambda_p^{-1}$ and $\psi_m^{IB} = 74°$ is most unstable with the growth rate $\gamma_m^{IB} = 0.19\Omega_p$; note that ψ_m^{IB} is far less than 90°. Figure 1b shows line plots of γ as a function of ω_r at $\psi = 0°$ and 74°. The AC instability (solid curve) has the maximum growth rate $\gamma_m^{AC} = 0.15\Omega_p$ at $\omega_r^{AC} = 0.63\Omega_p$. The local maxima of the IB instability growth rates are located just below their respective harmonic numbers, consistent with previous studies [e.g., *McClements et al.*, 1994; *Gary et al.*, 2011a].

Figure 2 displays time evolution of the field energies and component's/species' temperatures from the PIC simulation. Four selected times marked with $t_1 - t_4$ are at $30\Omega_p^{-1}$, $60\Omega_p^{-1}$, $90\Omega_p^{-1}$, and $150\Omega_p^{-1}$, respectively. The initial time step ($t = 0$) not shown will be denoted by t_0. Figure 3 shows the simulated magnetic (left column) and electric (right column) field power spectra in the k_x-k_y domain at the selected times. The superimposed white contours delineate the level of $\gamma = 0.1\Omega_p$ from linear theory calculation. Finally, Figure 4 shows four snapshots of the proton distribution, $f_p(t_i)$, normalized by the maximum of the initial proton ring, $\max(f_r(t_0))$ (left column), and the change of the distribution between t_i and t_{i-1} (right column) normalized by 4 $\max(f_r(t_0))$ (the factor 4 is applied to enhance the color contrast).

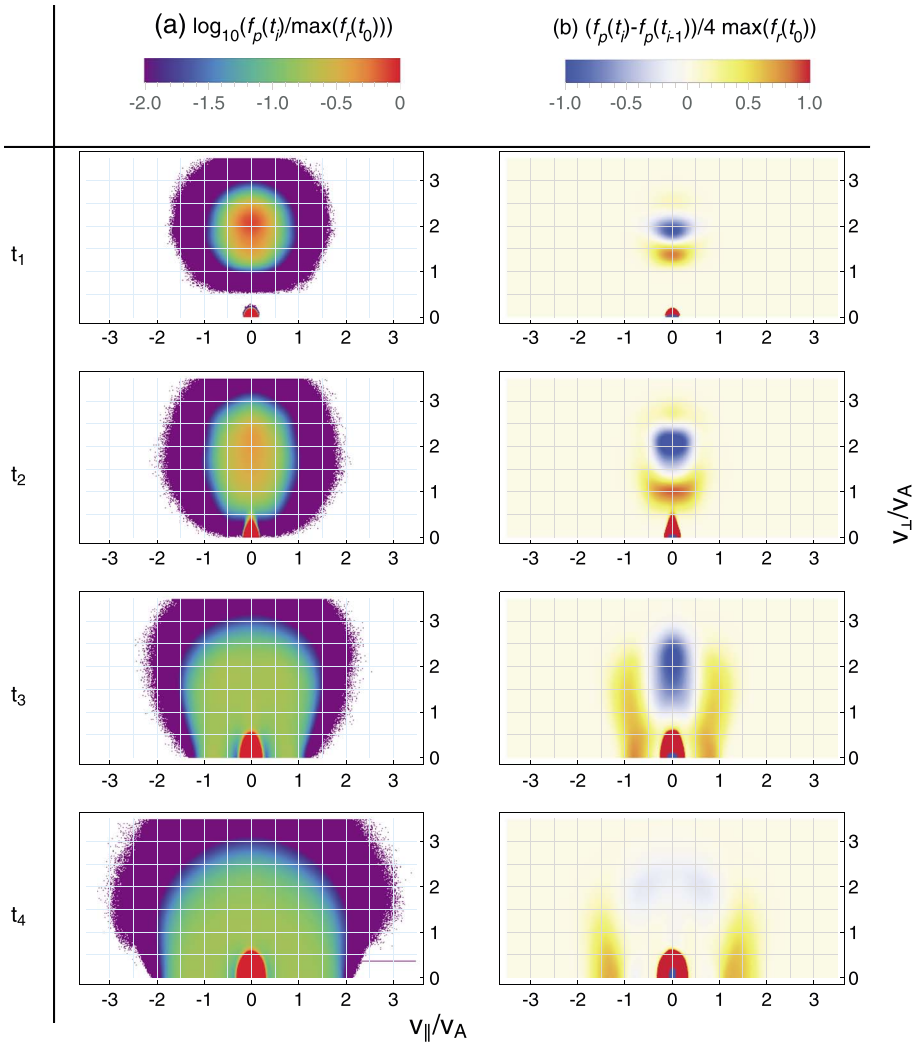

Figure 4. Four snapshots of the proton distribution f_p corresponding to $t_1 - t_4$ for model 1. (left column) $f_p(t_i)$ (in logarithmic scale) normalized by the maximum of $f_r(t_0)$, $\max(f_r(t_0))$; (right column) the change of f_p between two consecutive times normalized by 4 $\max(f_r(t_0))$. The saturated red color in the change plots means ≥ 1, whereas the saturated blue color means ≤ -1. The white regions in Figure 4 (left column) denote no proton zone.

Between time $t = 0$ and $30\Omega_p^{-1}$, the total energies of the electric and magnetic field fluctuations (black curves) linearly grow (in this log linear plot). During this phase, the in-plane perpendicular component of electric field energy ($\propto \delta E_y^2$) dominates, and the compressional and out-of-plane perpendicular components of magnetic field energy are comparable to each other and greater than the in-plane perpendicular component ($\delta B_x^2 \gtrsim \delta B_z^2 \gg \delta B_y^2$). These are the signatures of the IB modes propagating quasi-perpendicular to $\mathbf{B}_0$ [e.g., *Gary et al.*, 2010; *Liu et al.*, 2011a; *Min and Liu*, 2015b] which grow fastest in the system. The snapshots of the power spectra at t_1 show the enhanced IB modes within the contours of $\gamma = 0.1\Omega_p$, but no significant AC mode wave power is present yet. The harmonic structure is quite obvious for $k_x\lambda_p \lesssim 1$, but above $k_x\lambda_p \approx 1$ the spectra become continuous as predicted. From Figures 2c and 2d, the temperatures of the two proton components during this period have barely changed.

From then until $t \approx 50\Omega_p^{-1}$, the IB mode energy saturates followed by gradual decay. Comparing with the power spectra at t_1, the wave power of the IB modes for $k_y\lambda_p \gtrsim 5$ is substantially diminished at t_2. In contrast, the lower harmonic modes (roughly below the 5th harmonic) continue in growing. Also apparent during this period is the substantial scattering of protons predominantly along the perpendicular velocity component (Figure 4, second row). The background protons have gained substantial perpendicular energy [*Curtis*, 1985; *Horne et al.*, 2000] evidenced by the dark red, cone-shaped structure at the origin, and the ring protons have

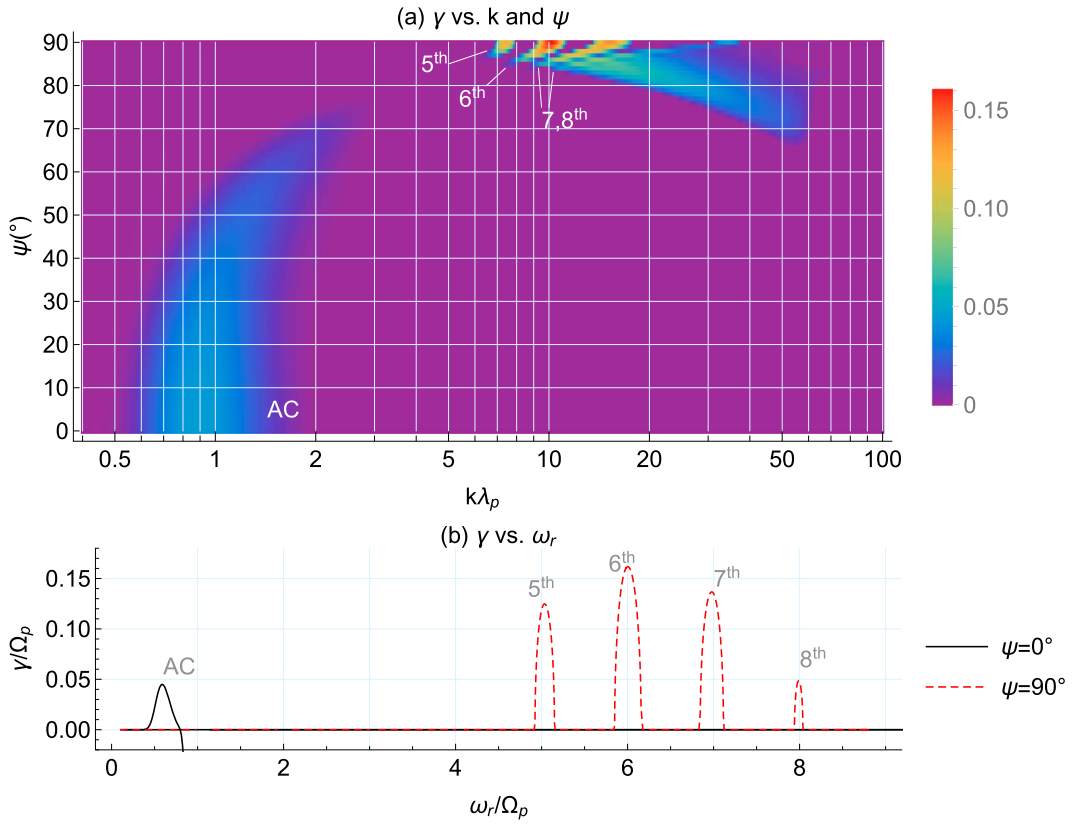

Figure 5. Linear theory results for model 2. The figure format is the same as Figure 1. Labels 5th–8th here denote the corresponding harmonic numbers of the IB modes.

been scattered into both decreasing and, at a lesser extent, increasing $v_\perp$ about $v_\perp \approx 2v_A$ where the ring distribution function of equation (1) initially peaked. Notably, the background electrons experienced rapid parallel heating (dash-dotted curve in Figure 2c) which appears to be nonphysical (more discussion in the next section).

During this period, the AC modes also grow out of the noise floor within the predicted wave number range, but proton pitch angle scattering has not yet stood out. There is another enhanced mode that was not predicted from linear theory, which is marked with W in Figure 3. This mode intensifies roughly right after the IB modes saturate and lies on the low-frequency portion of the whistler dispersion surface (not shown). Further test simulations demonstrated that their wave numbers change with the spatial resolution of the simulation (not shown), suggesting that they are numerical noises and nonphysical.

The period between t_2 and t_3 is featured by the linear growth phase of the AC instability, as evidenced by the roughly linear increase of the y and z components of the magnetic field energies. At time t_3, the magnetic field wave power spectrum peaks at $k_y\lambda_p \approx 0$. On the other hand, the wave power of the 4th harmonic and beyond of the IB modes is now substantially reduced, indicating that their free energy source has been exhausted. During this period, Figures 2c and 2d show that $T_{\perp r}/T_{\parallel r}$ of the ring protons has dropped from ~ 15 to ~ 4, while $T_{\parallel r}$ has increased significantly. The background protons further gained perpendicular energy perhaps from the remnant IB modes. Using numbers from Table 1, the parallel speed of protons in resonance with the most unstable AC mode propagating parallel to $\mathbf{B}_0$ is $v_{\parallel \mathrm{res}} \approx (\omega_{r,m}^{\mathrm{AC}} - \Omega_p)/k_m^{\mathrm{AC}} = -0.4v_A$. The change of the proton distribution between t_2 and t_3 shows the signature of pitch angle scattering, and the scattering occurs about $|v_\parallel| \sim 0.5v_A$ (due to the symmetry of the system), which is roughly consistent with the estimated $|v_{\parallel \mathrm{res}}|$.

The period between t_3 and t_4 is somewhat interesting because the magnetic field energy after saturation has remained relatively unchanged. Figures 2c and 2d show that the rates at which $T_{\parallel r}$ increases and $T_{\perp r}/T_{\parallel r}$ decreases (red curves) suddenly change at t_3, and Figure 3 (fourth row) shows that the maximum power of the

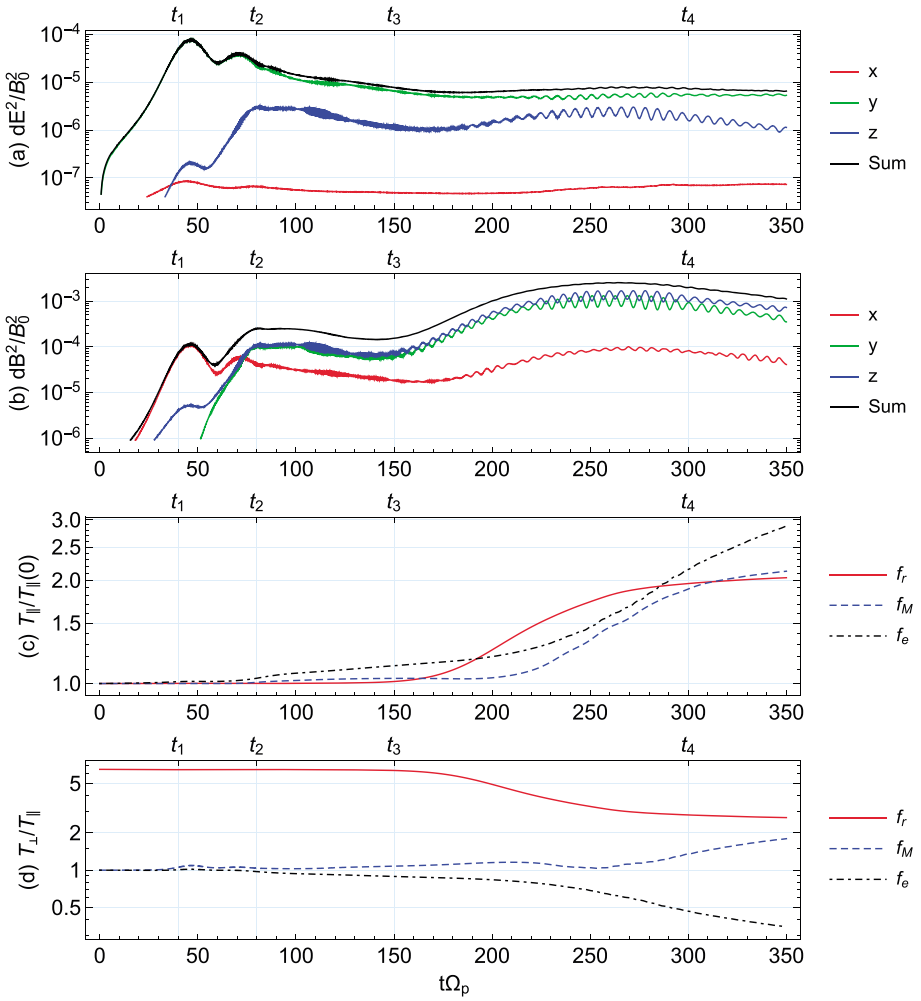

Figure 6. Time evolution of the simulated field energies and particle temperatures for model 2. The figure format is the same as Figure 2. Four selected times $t_1 - t_4$ marked here are at $40\Omega_p^{-1}$, $80\Omega_p^{-1}$, $150\Omega_p^{-1}$, and $300\Omega_p^{-1}$, respectively.

AC mode has migrated toward smaller k_x ($k_x \approx 0.6\lambda_p^{-1}$ at t_4). Figure 4 (fourth row) shows pronounced pitch angle scattering of the ring protons which have already filled the region $|v_\parallel| \gtrsim v_A$ initially devoid of protons there. As a result, the original ring distribution has become nearly isotropic; the temperature anisotropy at the end of the simulation run is $T_\perp/T_\parallel \approx 1.8$. Assuming that the phase speed of the dominant AC mode has changed little from t_3 (since ω_r decreases as well), the decrease of k_x results in the increase of $|v_{\parallel\text{res}}|$. Since the strongest AC mode at t_4 has $k_x\lambda_p \approx 0.6$, the resonant speed is $|v_{\parallel\text{res}}| \approx v_A$, roughly consistent with $|v_\parallel| \sim v_A$ about which the scattering occurs as shown in Figure 4 (fourth row). From Figure 3 (fourth row), the IB modes have been completely damped away by the time of t_4.

3.2. Small Ring Speed (Model 2)

Figure 5 displays the linear instability results for proton model 2. Compared to the previous case, there are several differences worth mentioning. First, the maximum growth rate of the AC instability ($\gamma_m^{\text{AC}} = 0.045\Omega_p$) is substantially reduced, which can be understood by the smaller ring proton anisotropy. On the other hand, the AC instability can be unstable up to $\psi \approx 70°$ (as opposed to $\psi \approx 60°$ for model 1). Second, the IB modes up to the 4th harmonic are stable at all propagation directions, related to the smaller ring speed [*Horne et al.*, 2000; *Chen et al.*, 2010b]. Last, the range of ψ of the IB instability is substantially limited to quasi-perpendicular propagation ($\psi \gtrsim 70°$), and the most unstable IB mode ($\gamma_m^{\text{IB}} = 0.16\Omega_p$) that is the 6th harmonic ($\omega_{r,m}^{\text{IB}} = 6\Omega_p$) propagates perpendicular to $\mathbf{B}_0$. However, there also exists the frequency continuum beyond the 8th harmonic as ψ decreases. Figure 5b shows line plots of γ versus ω_r for $\psi = 0°$ and 90°. Note that γ_m^{AC} is smaller by a factor of 3 than that of model 1, while γ_m^{IB} remains relatively unchanged.

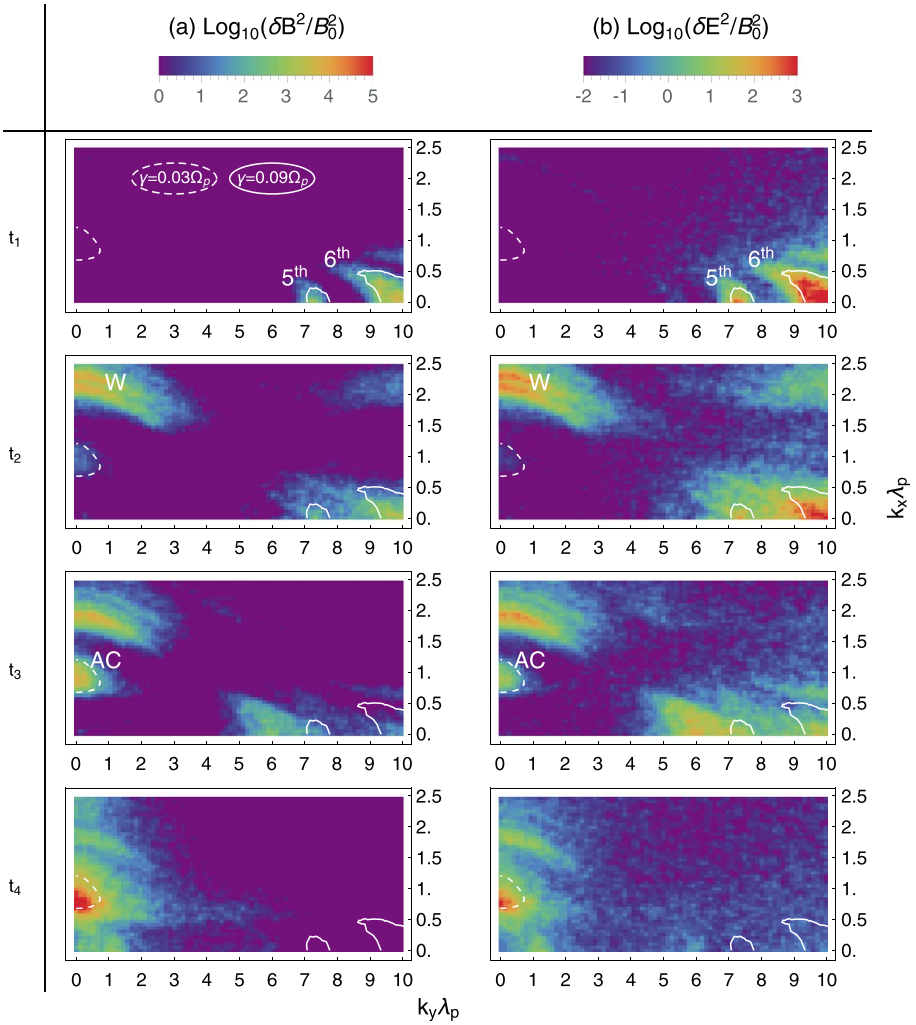

Figure 7. Four snapshots of simulated wave power spectra corresponding to $t_1 - t_4$ for model 2. The figure format is the same as Figure 3. Here the white dashed contours delineate the linear growth rates of $\gamma = 0.03\Omega_p$ and the solid contours delineate $\gamma = 0.09\Omega_p$, and labels 5th and 6th denote the corresponding harmonic number of the IB modes.

Figure 6 displays time evolution of field energies and particle temperatures. The four time steps $t_1 - t_4$ marked are $40\Omega_p^{-1}$, $80\Omega_p^{-1}$, $150\Omega_p^{-1}$, and $300\Omega_p^{-1}$, respectively. The time evolution of the field energies is roughly consistent with that of model 1, but the saturation levels of electric and magnetic field energies are roughly an order of magnitude smaller (for both the AC and IB instabilities). The quasi-electrostatic IB modes grow first until $t = 45\Omega_p^{-1}$ at which they saturate and start to decay. Unlike the model 1 case, these modes are predominantly compressional ($\delta B_x^2 > \delta B_z^2 \gg \delta B_y^2$), consistent with the more quasi-perpendicular propagation of the growing IB modes [e.g., *Gary et al.*, 2010, Figure 3]. Between $t \approx 60\Omega_p^{-1}$ and $t \approx 130\Omega_p^{-1}$, strong electromagnetic modes appear, which are the nonphysical low-frequency whistler mode noise also present in the case of model 1. This mode here stands out more clearly due to the lower saturation level of the IB modes. From then until $t = 260\Omega_p^{-1}$, the AC modes emerge and eventually saturate, and after that they gradually decay.

Figure 7 displays snapshots of the simulated wave power spectra at the four time steps. The dashed and solid contours delineate the $\gamma = 0.03\Omega_p$ level for the AC instability and the $\gamma = 0.09\Omega_p$ level for the IB instability, respectively. At time t_1, the 5th and 6th harmonic modes appear distinctly with slightly smaller k_y than predicted. The reason for this mismatch is that the simulation grid size along the y direction is not small enough to well resolve these high k_y modes. Nevertheless, the wave properties are generally consistent with the linear theory prediction. From then, it takes a while for the AC modes to emerge and finally saturate at t_3 due to the small growth rate. By this time, the IB modes are almost completely damped. Finally at t_4 and possibly

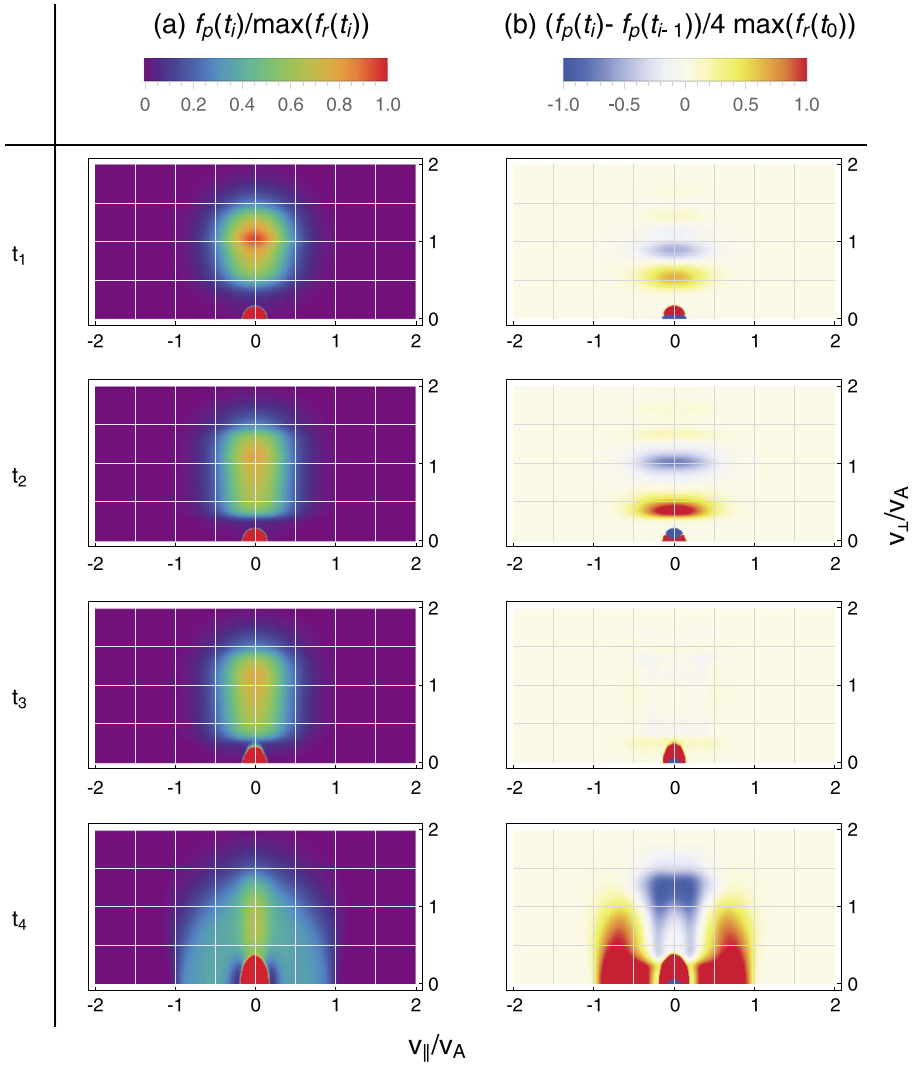

Figure 8. Four snapshots of the proton distribution f_p corresponding to $t_1 - t_4$ for model 2. The figure format is the same as Figure 4 except that f_p on Figure 8 (left column) is in linear scale.

thereafter, the dominant AC mode migrates toward smaller k_x as the ring proton distribution self-consistently evolves.

Figure 8 displays snapshots of the proton distribution. Consistent with the model 1 case, the ring protons lose energy through the predominant perpendicular velocity scattering by IB modes until t_2 and, at the same time, the background protons gain some perpendicular energy. From then until t_3, the IB modes continue to damp out while the AC modes have not yet grown up. The system is dominated by the nonphysical whistler mode noise as discussed above. These whistler modes do not effectively resonate with protons. Accordingly, the change in the proton distribution during this phase is negligible, as evidenced by the change plot at t_3 in Figure 8. Between t_3 and t_4, AC modes grow above the whistler mode noise. The ring protons lose energy through the pitch angle scattering as the cyclotron resonance with parallel propagating AC waves operates. The predicted resonant speed for the most unstable AC mode is, using the parameters in Table 1, $|v_{\parallel res}| = 0.45v_A$. The resonant speed revealed by the change plot at t_4 in Figure 8 appears to be close to this value. By the time of t_4, the ring protons have been substantially isotropized, but substantial ring protons still remain near $v_\parallel \approx 0$. This is different from the proton distribution of the model 1 case at the end of the simulation. The reason is that the AC modes here have much smaller growth rates and the wave saturate level is also an order of magnitude lower. Subsequently, a much longer time is needed for the proton distribution to be fully isotropized.

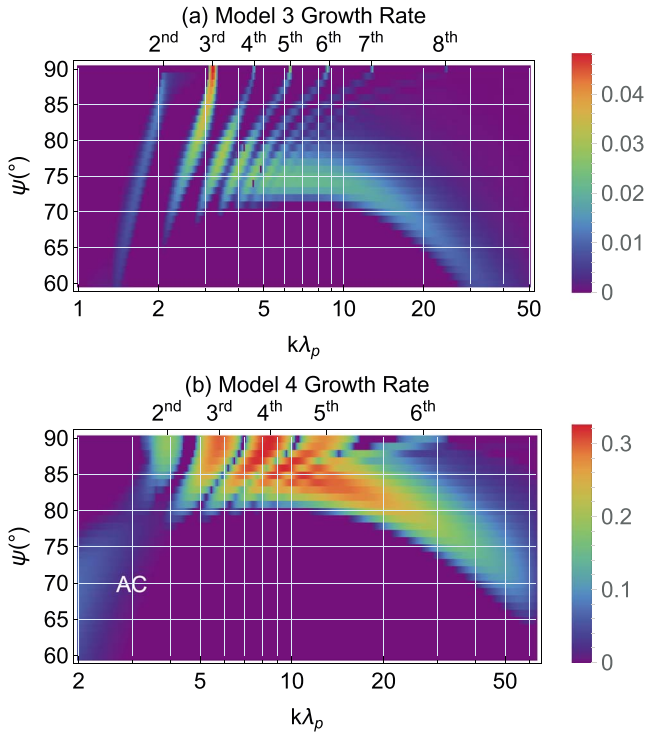

Figure 9. Linear growth rate γ/Ω_p focused on the IB instability as a function of $\psi(°)$ and $k\lambda_p$ for models (a) 3 and (b) 4. Label AC denotes the AC instability extending to large ψ.

4. Discussions

A notable difference between the IB instabilities of models 1 and 2 is the wave normal angle of the maximum growing mode, ψ_m^{IB}. The only difference of the two proton models discussed in the previous section is the ring speed. Here we further examine the dependence of ψ_m^{IB} on the ring concentration n_r/n_e. Figure 9a displays the linear growth rate of the IB instability for $n_r/n_e = 0.01$ and $v_r/v_A = 2$ (model 3). In contrast to the model 1 case, the maximum growth rate ($\gamma_m^{\mathrm{IB}} = 0.049\Omega_p$) appears at the 3rd harmonic and $\psi_m^{\mathrm{IB}} = 90°$. Interestingly though, the growth rate pattern shown in Figure 9a is very consistent with that in Figure 1a, but apparently, scaling of γ to n_r/n_e is not uniform with respect to k and ψ. The same linear instability analysis was carried out for $n_r/n_e = 0.5$ (model 5). As shown in Table 1, ψ_m^{IB} varies only slightly compared to the model 1 results. Figure 9b displays the linear growth rate of the IB instability for $n_r/n_e = 0.5$ and $v_r/v_A = 1$ (model 4). Despite the huge increase of n_r/n_e, ψ_m^{IB} remains to be 90° (Table 1). However, a pronounced difference is the shift of the unstable harmonics at $\psi \sim 90°$. For model 2, the lower harmonics were all stable, but with increased n_r/n_e for model 4 the lower harmonics now become unstable, while the higher harmonics become stable.

A counterintuitive result in the PIC simulations is the larger saturation level of the AC waves, despite their smaller linear growth rate. A likely explanation is that there is more free energy available for the AC waves to grow. Figure 10 displays line plots of the electromagnetic energy density of the simulated fluctuations (ε_{EB}, red) and the variation of the kinetic energy density of the ring protons from their initial kinetic energy density ($\Delta\varepsilon_r$, black) for models (a) 1 and (b) 2. Apparently, the loss of the kinetic energy of the ring protons ($\Delta\varepsilon_r < 0$) is associated with the gain of the electromagnetic wave energy ($\varepsilon_{EB} > 0$), although $|\Delta\varepsilon_r| > \varepsilon_{\mathrm{EB}}$ since the energy gain of the background protons and electrons has not been accounted for. The two local peaks of $\varepsilon_{\mathrm{EB}}$ are marked with the vertical lines at t_{IB} and t_{AC} in each plot, corresponding to the times at which the IB and AC modes saturate, respectively. In both cases, the decrease of $\Delta\varepsilon_r$ between t_{IB} and t_{AC} is much larger than that between t_0 and t_{IB} (i.e., $\varepsilon_r(t_{\mathrm{IB}}) - \varepsilon_r(t_{\mathrm{AC}}) > \varepsilon_r(t_0) - \varepsilon_r(t_{\mathrm{IB}})$). This difference is almost an order of magnitude for model 2, which can explain $\varepsilon_{EB}(t_{\mathrm{AC}})/\varepsilon_{EB}(t_{\mathrm{IB}}) \gtrsim 10$ in this model. Consequently, the AC waves gain more energy and thereby saturate at a higher level than the IB modes.

In both cases presented, although the AC waves start to emerge after the IB waves have developed and saturated, their properties are not much affected by the development of the IB waves. The initial growth of

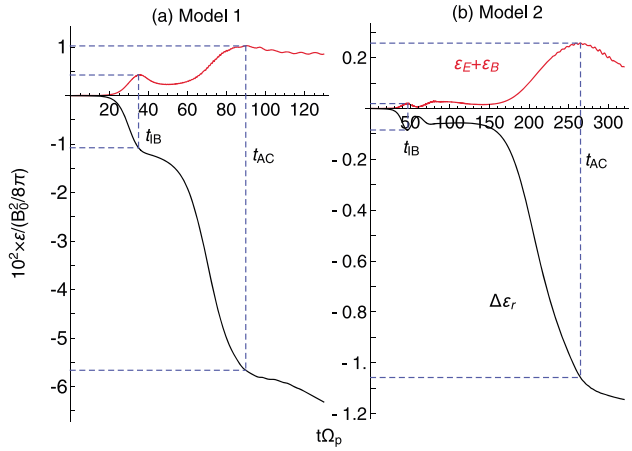

Figure 10. Time evolution of the energy density of the simulated electromagnetic fluctuations ($\varepsilon_{EB} = \varepsilon_E + \varepsilon_B$, red) and difference of the kinetic energy density of the ring protons from the initial kinetic energy ($\Delta\varepsilon_r$, black) for models (a) 1 and (b) 2. The energy density is normalized to $\mathbf{B}_0^2/8\pi$. Labels t_1 and t_2 mark the first and second local peaks of ε_{EB}, respectively.

the AC modes occurs within the wave number range predicted by linear theory based on the initial proton distribution. As described in the previous section as well as shown in Figures 2 and 6, the scattering of the ring protons by the IB waves predominantly occur in the perpendicular velocity component which does not lead to substantial changes in $T_{\|r}$ and $T_{\perp r}$. Accordingly, the AC waves developed next do not differ significantly from the linear theory prediction based on the initial proton distribution. However, it is clear that as the proton distribution further evolves, the enhanced AC waves gradually migrate toward longer wavelength (Figures 3 and 7).

The present study has implications on the proton ring-like velocity distributions associated with the fast magnetosonic waves observed in the inner magnetosphere. As suggested by the results, if these proton velocity distributions are very anisotropic ring distributions like our model distributions, EMIC waves will dominate the observed waves in situ and fast magnetosonic waves will be, if detected at all, weaker. In contrast, if these ring-like proton velocity distributions are nearly isotropic and close to shell velocity distributions [e.g., *Gary et al.*, 2010; *Liu et al.*, 2011a; *Min and Liu*, 2015a], the Alfvén-cyclotron instability becomes stable and EMIC waves will not grow to a sufficient level. Since fast magnetosonic waves and EMIC waves are often observed separately in the inner magnetosphere, the distributions responsible for the fast magnetosonic waves observed should be more isotropic partial-shell distributions instead of the ring distributions used.

Another result worth mentioning is the harmonic-dependent evolution of the IB modes; as shown in Figure 3 the IB modes of smaller k (or equivalently smaller ω_r) last longer. To better understand this harmonic-dependent evolution, Figure 11 (top) displays the frequency-time spectrogram of the simulated electric field fluctuations for model 1, sampled at a single point in space, equivalent to a frequency-time spectrogram from a single satellite (more precisely, several such spectrograms at multiple points were averaged to minimize the background noise). A Hanning window of length $t = 40\Omega_p^{-1}$ moving in steps of Ω_p^{-1} was applied to each component of $\delta\mathbf{E}$. Figure 11 (bottom) displays vertical slices of the spectrogram at $t = 35\Omega_p^{-1}$, $55\Omega_p^{-1}$, and $75\Omega_p^{-1}$. Clearly, the timescale of the high-frequency modes is shorter than that of the low-frequency modes. Considering that satellites would more likely measure the lingering field fluctuations, chances are that the linear growth rate of the IB instability shown in Figure 1b would not reflect actual wave amplitude per se. On the other hand, our simulations are concerned with the evolution of fields and particles in a closed system given an initially prescribed proton ring distribution, as opposed to the realistic situation in which protons of the ring distribution can be continuously injected into the system [cf. *Denton et al.*, 1993; *Liu et al.*, 2012]. In such a case, correlation between the linear growth rate and the corresponding amplitude of fast magnetosonic waves may be good, and several observations have indeed shown cases of good agreement [e.g., *Balikhin et al.*, 2015].

It has been shown that the thermal and suprathermal electrons can interact with ion Bernstein or fast magnetosonic waves through Landau resonance [*Horne et al.*, 2000, 2007; *Gary et al.*, 2011a]. However, the rapid

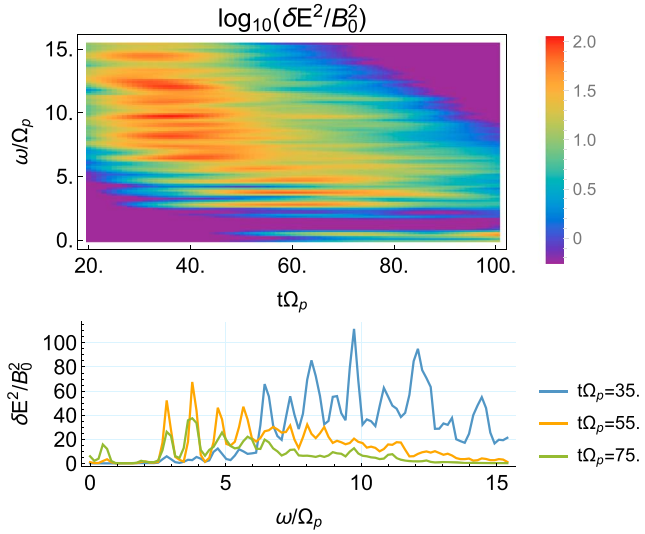

Figure 11. (top) Frequency-time spectrogram and (bottom) frequency spectrum of the simulated electric field fluctuations for model 1. The three curves in Figure 11 (bottom) are vertical slices of Figure 11 (top) at $t = 35\Omega_p^{-1}$, $55\Omega_p^{-1}$, and $75\Omega_p^{-1}$, respectively.

parallel electron heating observed in the PIC simulations (Figures 2 and 6) does not appear to be caused by the IB modes at quasi-perpendicular propagation. For example, in model 1, the Landau resonant speed of the most unstable IB mode (from Table 1) is $\omega_{r,m}^{IB}/(k_{\|m}^{IB}) = 9.7/(7.06\cos 74°) \approx 5v_A$. This is much higher than the thermal speed of the background electrons ($\theta_e \approx 0.45v_A$). We initially used 250 simulation particles per cell, and component/species in the simulations and the electron heating appeared. Subsequently, we increased the number of the simulation particles by a factor of 10 because we suspected that the thermal noise due to the small number of simulation particles might have caused the anomalous electron heating. Interestingly, while the simulation results remain very consistent with the runs using less simulation particles, the significant parallel electron heating still persists (not shown). It is still unclear what exactly causes the electron heating. We should, on the other hand, emphasize that the main simulation results presented are not much affected by this anomalous electron heating.

5. Summary

In this study, the properties of the Alfvén-cyclotron (AC) and ion Bernstein (IB) instabilities driven by a proton ring velocity distribution have been studied using linear kinetic dispersion theory and two-dimensional electromagnetic PIC simulations. For systematic analyses, a simplified two-component proton velocity distribution consisting of a 10% ring distribution and a 90% thermal background is assumed for the proton distribution. Two cases with ring speeds $v_r/v_A = 1$ and 2 have been examined. The primary results are summarized as follows.

1. For both cases, the maximum growth rate γ_m of the IB instability is larger than that of the AC instability. Furthermore, γ_m of the AC instability is sensitive to v_r (due to $T_\perp/T_\| \propto v_r^2$), while γ_m of the IB instability is not. The most unstable AC mode propagates parallel to $\mathbf{B}_0$ independent of the ring concentrations n_r/n_e considered here, but the most unstable IB mode can exhibit a transition of the wave normal angle away from 90° with increasing n_r/n_e.
2. The corresponding two-dimensional PIC simulations confirm the linear theory results for the growth rates of both the AC and IB instabilities. The IB modes develop and saturate first, and the growth and saturation of the AC modes follow later with strong electromagnetic fluctuations. However, in both cases, the saturation level of the AC modes is larger than that of the IB modes, despite the larger growth rate of the latter modes.
3. The simulations also reveal two distinct types of ring proton scattering, namely, perpendicular velocity scattering associated with the IB instability and pitch angle scattering associated with the AC instability. Close examination of the ring proton distribution reveals that the perpendicular velocity scattering results in proton transport toward both smaller and, at a lesser extent, larger perpendicular velocity without causing

substantial change of either the parallel temperature or the temperature anisotropy of the ring protons. Furthermore, free energy resulting from the pitch angle scattering is larger than that resulting from the perpendicular velocity scattering, thereby leading to larger saturation level of the AC modes.

Acknowledgments
Data supporting the figures presented are available upon request from the corresponding author. The work at Auburn University was supported by NASA grant NNX13AD62G and NSF grant 1303623. Computational resources supporting this work were provided by the NASA High-End Computing (HEC) Program through the NASA Advanced Supercomputing (NAS) Division at Ames Research Center. Authors thank S. Peter Gary for the constructive suggestions.

References

Balikhin, M. A., Y. Y. Shprits, S. N. Walker, L. Chen, N. Cornilleau-Wehrlin, I. Dandouras, O. Santolík, C. Carr, K. H. Yearby, and B. Weiss (2015), Observations of discrete harmonics emerging from equatorial noise, *Nat. Commun.*, *6*, 7703, doi:10.1038/ncomms8703.

Birdsall, C. K., and A. B. Langdon (1985), *Plasma Physics via Computer Simulation*, McGraw-Hill, New York.

Blum, L. W., E. A. MacDonald, S. P. Gary, M. F. Thomsen, and H. E. Spence (2009), Ion observations from geosynchronous orbit as a proxy for ion cyclotron wave growth during storm times, *J. Geophys. Res.*, *114*, A10214, doi:10.1029/2009JA014396.

Blum, L. W., E. A. MacDonald, L. B. N. Clausen, and X. Li (2012), A comparison of magnetic field measurements and a plasma-based proxy to infer EMIC wave distributions at geosynchronous orbit, *J. Geophys. Res.*, *117*, A05220, doi:10.1029/2011JA017474.

Boardsen, S. A., D. L. Gallagher, D. A. Gurnett, W. K. Peterson, and J. L. Green (1992), Funnel-shaped, low-frequency equatorial waves, *J. Geophys. Res.*, *97*(A10), 14,967–14,976, doi:10.1029/92JA00827.

Bortnik, J., and R. M. Thorne (2010), Transit time scattering of energetic electrons due to equatorially confined magnetosonic waves, *J. Geophys. Res.*, *115*, A07213, doi:10.1029/2010JA015283.

Chen, L. (2015), Wave normal angle and frequency characteristics of magnetosonic wave linear instability, *Geophys. Res. Lett.*, *42*, 4709–4715, doi:10.1002/2015GL064237.

Chen, L., R. M. Thorne, V. K. Jordanova, C.-P. Wang, M. Gkioulidou, L. Lyons, and R. B. Horne (2010a), Global simulation of EMIC wave excitation during the 21 April 2001 storm from coupled RCM-RAM-HOTRAY modeling, *J. Geophys. Res.*, *115*, A07209, doi:10.1029/2009JA015075.

Chen, L., R. M. Thorne, V. K. Jordanova, and R. B. Horne (2010b), Global simulation of magnetosonic wave instability in the storm time magnetosphere, *J. Geophys. Res.*, *115*, A11222, doi:10.1029/2010JA015707.

Chen, L., R. M. Thorne, V. K. Jordanova, M. F. Thomsen, and R. B. Horne (2011), Magnetosonic wave instability analysis for proton ring distributions observed by the LANL magnetospheric plasma analyzer, *J. Geophys. Res.*, *116*, A03223, doi:10.1029/2010JA016068.

Chen, L., A. Maldonado, J. Bortnik, R. M. Thorne, J. Li, L. Dai, and X. Zhan (2015), Nonlinear bounce resonances between magnetosonic waves and equatorially mirroring electrons, *J. Geophys. Res. Space Physics*, *120*, 6514–6527, doi:10.1002/2015JA021174.

Cornwall, J. M. (1965), Cyclotron instabilities and electromagnetic emission in the ultra low frequency and very low frequency ranges, *J. Geophys. Res.*, *70*(1), 61–69, doi:10.1029/JZ070i001p00061.

Curtis, S., and C. Wu (1979), Gyroharmonic emissions induced by energetic ions in the equatorial plasmasphere, *J. Geophys. Res.*, *84*(A6), 2597–607, doi:10.1029/JA084iA06p02597.

Curtis, S. A. (1985), Equatorial trapped plasmasphere ion distributions and transverse stochastic acceleration, *J. Geophys. Res.*, *90*(A2), 1765–1770, doi:10.1029/JA090iA02p01765.

Denton, R. E., M. K. Hudson, S. A. Fuselier, and B. J. Anderson (1993), Electromagnetic ion cyclotron waves in the plasma depletion layer, *J. Geophys. Res.*, *98*(A8), 13,477–13,490, doi:10.1029/93JA00796.

Denton, R. E., M. J. Engebretson, A. Keiling, A. P. Walsh, S. P. Gary, P. M. E. Décréau, C. A. Cattell, and H. Rème (2010), Multiple harmonic ULF waves in the plasma sheet boundary layer: Instability analysis, *J. Geophys. Res.*, *115*, A12224, doi:10.1029/2010JA015928.

Denton, R. E., V. K. Jordanova, and B. J. Fraser (2014), Effect of spatial density variation and O+ concentration on the growth and evolution of electromagnetic ion cyclotron waves, *J. Geophys. Res. Space Physics*, *119*, 8372–8395, doi:10.1002/2014JA020384.

Denton, R. E., V. K. Jordanova, and J. Bortnik (2015), Resonance of relativistic electrons with electromagnetic ion cyclotron waves, *Geophys. Res. Lett.*, *42*, 8263–8270, doi:10.1002/2015GL064379.

Fu, X., et al. (2014), Whistler anisotropy instabilities as the source of banded chorus: Van Allen Probes observations and particle-in-cell simulations, *J. Geophys. Res. Space Physics*, *119*, 8288–8298, doi:10.1002/2014JA020364.

Gamayunov, K. V., and G. V. Khazanov (2008), Crucial role of ring current H+ in electromagnetic ion cyclotron wave dispersion relation: Results from global simulations, *J. Geophys. Res.*, *113*, A11220, doi:10.1029/2008JA013494.

Gary, S. P., M. B. Moldwin, M. F. Thomsen, D. Winske, and D. J. McComas (1994), Hot proton anisotropies and cool proton temperatures in the outer magnetosphere, *J. Geophys. Res.*, *99*(A12), 23,603–23,615, doi:10.1029/94JA02069.

Gary, S. P., K. Liu, D. Winske, and R. E. Denton (2010), Ion Bernstein instability in the terrestrial magnetosphere: Linear dispersion theory, *J. Geophys. Res.*, *115*, A12209, doi:10.1029/2010JA015965.

Gary, S. P., K. Liu, and D. Winske (2011a), Bernstein instability driven by suprathermal protons in the ring current, *J. Geophys. Res.*, *116*, A08215, doi:10.1029/2011JA016543.

Gary, S. P., K. Liu, and D. Winske (2011b), Whistler anisotropy instability at low electron beta: Particle-in-cell simulations, *Phys. Plasmas*, *18*(8), 082902, doi:10.1063/1.3610378.

Gary, S. P., K. Liu, and L. Chen (2012), Alfvén-cyclotron instability with singly ionized helium: Linear theory, *J. Geophys. Res.*, *117*, A08201, doi:10.1029/2012JA017740.

Gendrin, R., M. Ashour-Abdalla, Y. Omura, and K. Quest (1984), Linear analysis of ion cyclotron interaction in a multicomponent plasma, *J. Geophys. Res.*, *89*(A10), 9119–9124, doi:10.1029/JA089iA10p09119.

Gomberoff, L., and R. Neira (1983), Convective growth rate of ion cyclotron waves in a H^+/He^+ and $H^+/He^{++}/O^+$ plasma, *J. Geophys. Res.*, *88*, 2170–2174, doi:10.1029/JA088iA03p02170.

Gul'elmi, A., B. Klaine, and A. Potapov (1975), Excitation of magnetosonic waves with discrete spectrum in the equatorial vicinity of the plasmapause, *Planet. Space Sci.*, *23*(2), 279–286, doi:10.1016/0032-0633(75)90133-6.

Gurnett, D. A. (1976), Plasma wave interactions with energetic ions near the magnetic equator, *J. Geophys. Res.*, *81*(16), 2765–2770, doi:10.1029/JA081i016p02765.

Horne, R., and R. Thorne (1994), Convective instabilities of electromagnetic ion cyclotron waves in the outer magnetosphere, *J. Geophys. Res.*, *99*(A9), 17,259–17,273, doi:10.1029/94JA01259.

Horne, R. B., G. V. Wheeler, and H. S. C. K. Alleyne (2000), Proton and electron heating by radially propagating fast magnetosonic waves, *J. Geophys. Res.*, *105*(A12), 27,597–27,610, doi:10.1029/2000JA000018.

Horne, R. B., R. M. Thorne, S. A. Glauert, N. P. Meredith, D. Pokhotelov, and O. Santolík (2007), Electron acceleration in the Van Allen radiation belts by fast magnetosonic waves, *Geophys. Res. Lett.*, *34*, L17107, doi:10.1029/2007GL030267.

Hrbáčková, Z., O. Santolík, F. Němec, E. Macúšová, and N. Cornilleau-Wehrlin (2015), Systematic analysis of occurrence of equatorial noise emissions using 10 years of data from the Cluster mission, *J. Geophys. Res. Space Physics*, *120*, 1007–1021, doi:10.1002/2014JA020268.

Hu, Y., R. E. Denton, and J. R. Johnson (2010), Two-dimensional hybrid code simulation of electromagnetic ion cyclotron waves of multi-ion plasmas in a dipole magnetic field, *J. Geophys. Res.*, *115*, A09218, doi:10.1029/2009JA015158.

Jordanova, V. K., J. U. Kozyra, A. F. Nagy, and G. V. Khazanov (1997), Kinetic model of the ring current-atmosphere interactions, *J. Geophys. Res.*, *102*(A7), 14,279–14,291, doi:10.1029/96JA03699.

Jordanova, V. K., C. J. Farrugia, R. M. Thorne, G. V. Khazanov, G. D. Reeves, and M. F. Thomsen (2001), Modeling ring current proton precipitation by electromagnetic ion cyclotron waves during the May 14–16, 1997, storm, *J. Geophys. Res.*, *106*(A1), 7–22, doi:10.1029/2000JA002008.

Kasahara, Y., H. Kenmochi, and I. Kimura (1994), Propagation characteristics of the ELF emissions observed by the satellite Akebono in the magnetic equatorial region, *Radio Sci.*, *29*(4), 751–767, doi:10.1029/94RS00445.

Kennel, C. F., and H. E. Petschek (1966), Limit on stably trapped particle fluxes, *J. Geophys. Res.*, *71*(1), 1–28, doi:10.1029/JZ071i001p00001.

Kersten, T., R. B. Horne, S. A. Glauert, N. P. Meredith, B. J. Fraser, and R. S. Grew (2014), Electron losses from the radiation belts caused by EMIC waves, *J. Geophys. Res. Space Physics*, *119*, 8820–8837, doi:10.1002/2014JA020366.

Khazanov, G. V., K. V. Gamayunov, D. L. Gallagher, and J. U. Kozyra (2006), Self-consistent model of magnetospheric ring current and propagating electromagnetic ion cyclotron waves: Waves in multi-ion magnetosphere, *J. Geophys. Res.*, *111*, A10202, doi:10.1029/2006JA011833.

Kozyra, J. U., T. E. Cravens, A. F. Nagy, E. G. Fontheim, and R. S. B. Ong (1984), Effects of energetic heavy ions on electromagnetic ion cyclotron wave generation in the plasmapause region, *J. Geophys. Res.*, *89*(A4), 2217–233, doi:10.1029/JA089iA04p02217.

Laakso, H., H. Junginger, A. Roux, R. Schmidt, and C. de Villedary (1990), Magnetosonic waves above f_c (H^+) at geostationary orbit: GEOS 2 results, *J. Geophys. Res.*, *95*(A7), 10,609–10,621, doi:10.1029/JA095iA07p10609.

Lee, J. H., and V. Angelopoulos (2014), Observations and modeling of EMIC wave properties in the presence of multiple ion species as function of magnetic local time, *J. Geophys. Res. Space Physics*, *119*, 8942–8970, doi:10.1002/2014JA020469.

Liu, K. (2007), Particle-in-cell simulations of particle energization in the auroral region, PhD thesis, Cornell Univ., New York.

Liu, K., S. P. Gary, and D. Winske (2011a), Excitation of magnetosonic waves in the terrestrial magnetosphere: Particle-in-cell simulations, *J. Geophys. Res.*, *116*, A07212, doi:10.1029/2010JA016372.

Liu, K., S. P. Gary, and D. Winske (2011b), Excitation of banded whistler waves in the magnetosphere, *Geophys. Res. Lett.*, *38*, L14108, doi:10.1029/2011GL048375.

Liu, K., E. Möbius, S. P. Gary, and D. Winske (2012), Pickup proton instabilities and scattering in the distant solar wind and the outer heliosheath: Hybrid simulations, *J. Geophys. Res.*, *117*, A10102, doi:10.1029/2012JA017969.

Loto'aniu, T. M., B. J. Fraser, and C. L. Waters (2005), Propagation of electromagnetic ion cyclotron wave energy in the magnetosphere, *J. Geophys. Res.*, *110*, A07214, doi:10.1029/2004JA010816.

Ma, Q., W. Li, L. Chen, R. M. Thorne, and V. Angelopoulos (2014), Magnetosonic wave excitation by ion ring distributions in the Earth's inner magnetosphere, *J. Geophys. Res. Space Physics*, *119*, 844–852, doi:10.1002/2013JA019591.

Ma, Q., et al. (2015), Modeling inward diffusion and slow decay of energetic electrons in the Earth's outer radiation belt, *Geophys. Res. Lett.*, *42*, 987–995, doi:10.1002/2014GL062977.

McClements, K. G., and R. O. Dendy (1993), Ion cyclotron harmonic wave generation by ring protons in space plasmas, *J. Geophys. Res.*, *98*(A7), 11,689–11,700, doi:10.1029/93JA00158.

McClements, K. G., R. O. Dendy, and C. N. Lashmore-Davies (1994), A model for the generation of obliquely propagating ULF waves near the magnetic equator, *J. Geophys. Res.*, *99*(A12), 23,685–23,693, doi:10.1029/94JA01979.

Meredith, N. P., M. Cain, R. B. Horne, R. M. Thorne, D. Summers, and R. R. Anderson (2003), Evidence for chorus-driven electron acceleration to relativistic energies from a survey of geomagnetically disturbed periods, *J. Geophys. Res.*, *108*(A6), 1248, doi:10.1029/2002JA009764.

Meredith, N. P., R. B. Horne, and R. R. Anderson (2008), Survey of magnetosonic waves and proton ring distributions in the Earth's inner magnetosphere, *J. Geophys. Res.*, *113*, A06213, doi:10.1029/2007JA012975.

Millan, R. M., and R. M. Thorne (2007), Review of radiation belt relativistic electron losses, *J. Atmos. Sol. Terr. Phys.*, *69*(3), 362–377, doi:10.1016/j.jastp.2006.06.019.

Min, K., and K. Liu (2015a), Fast magnetosonic waves driven by shell velocity distributions, *J. Geophys. Res. Space Physics*, *120*, 2739–2753, doi:10.1002/2015JA021041.

Min, K., and K. Liu (2015b), Regime transition of ion Bernstein instability driven by ion shell velocity distributions, *J. Geophys. Res. Space Physics*, *120*, 8448–8454, doi:10.1002/2015JA021514.

Min, K., et al. (2015), Study of EMIC wave excitation using direct ion measurements, *J. Geophys. Res. Space Physics*, *120*, 2702–2719, doi:10.1002/2014JA020717.

Mithaiwala, M., C. Crabtree, G. Ganguli, L. Rudakov, and K. Keika (2013), Convective amplification of electromagnetic ion cyclotron waves from ring-distribution protons in the inner magnetosphere, *J. Geophys. Res. Space Physics*, *118*, 7538–7544, doi:10.1002/2013JA019134.

Němec, F., O. Santolík, K. Gereová, E. Macúšová, Y. de Conchy, and N. Cornilleau-Wehrlin (2005), Initial results of a survey of equatorial noise emissions observed by the Cluster spacecraft, *Planet. Space Sci.*, *53*(1–3), 291–298, doi:10.1016/j.pss.2004.09.055.

Němec, F., O. Santolík, K. Gereová, E. Macúšová, H. Laakso, Y. de Conchy, M. Maksimovic, and N. Cornilleau-Wehrlin (2006), Equatorial noise: Statistical study of its localization and the derived number density, *Adv. Space Res.*, *37*(3), 610–616, doi:10.1016/j.asr.2005.03.025.

Omidi, N., R. M. Thorne, and J. Bortnik (2010), Nonlinear evolution of EMIC waves in a uniform magnetic field: 1. Hybrid simulations, *J. Geophys. Res.*, *115*, A12241, doi:10.1029/2010JA015607.

Perraut, S., A. Roux, P. Robert, R. Gendrin, J.-A. Sauvaud, J.-M. Bosqued, G. Kremser, and A. Korth (1982), A systematic study of ULF waves above f_{H+} from GEOS 1 and 2 measurements and their relationships with proton ring distributions, *J. Geophys. Res.*, *87*(A8), 6219–6236, doi:10.1029/JA087iA08p06219.

Posch, J. L., M. J. Engebretson, C. N. Olson, S. A. Thaller, A. W. Breneman, J. R. Wygant, S. A. Boardsen, C. A. Kletzing, C. W. Smith, and G. D. Reeves (2015), Low-harmonic magnetosonic waves observed by the Van Allen Probes, *J. Geophys. Res. Space Physics*, *120*, 6230–6257, doi:10.1002/2015JA021179.

Russell, C. T., R. E. Holzer, and E. J. Smith (1970), OGO 3 observations of ELF noise in the magnetosphere: 2. The nature of the equatorial noise, *J. Geophys. Res.*, *75*(4), 755–768, doi:10.1029/JA075i004p00755.

Santolík, O., J. S. Pickett, D. A. Gurnett, M. Maksimovic, and N. Cornilleau-Wehrlin (2002), Spatiotemporal variability and propagation of equatorial noise observed by Cluster, *J. Geophys. Res.*, *107*(A12), 1495, doi:10.1029/2001JA009159.

Santolík, O., F. Němec, K. Gereová, E. Macúšová, Y. de Conchy, and N. Cornilleau-Wehrlin (2004), Systematic analysis of equatorial noise below the lower hybrid frequency, *Ann. Geophys.*, *22*(7), 2587–2595, doi:10.5194/angeo-22-2587-2004.

Shprits, Y. Y., D. A. Subbotin, N. P. Meredith, and S. R. Elkington (2008), Review of modeling of losses and sources of relativistic electrons in the outer radiation belt II: Local acceleration and loss, *J. Atmos. Sol. Terr. Phys.*, *70*(14), 1694–1713, doi:10.1016/j.jastp.2008.06.014.

Shprits, Y. Y., D. Subbotin, A. Drozdov, M. E. Usanova, A. Kellerman, K. Orlova, D. N. Baker, D. L. Turner, and K.-C. Kim (2013), Unusual stable trapping of the ultrarelativistic electrons in the Van Allen radiation belts, *Nat. Phys.*, *9*, 699–703, doi:10.1038/nphys2760.

Thomsen, M. F., M. H. Denton, V. K. Jordanova, L. Chen, and R. M. Thorne (2011), Free energy to drive equatorial magnetosonic wave instability at geosynchronous orbit, *J. Geophys. Res.*, *116*, A08220, doi:10.1029/2011JA016644.

Umeda, T., S. Matsukiyo, T. Amano, and Y. Miyoshi (2012), A numerical electromagnetic linear dispersion relation for Maxwellian ring-beam velocity distributions, *Phys. Plasmas*, *19*(7), 072107, doi:10.1063/1.4736848.

Usanova, M. E., et al. (2014), Effect of EMIC waves on relativistic and ultrarelativistic electron populations: Ground-based and Van Allen Probes observations, *Geophys. Res. Lett.*, *41*, 1375–1381, doi:10.1002/2013GL059024.

Vandas, M., and P. Hellinger (2015), Linear dispersion properties of ring velocity distribution functions, *Phys. Plasmas*, *22*(6), 062107, doi:10.1063/1.4922073.

Viñas, A. F., R. L. Mace, and R. F. Benson (2005), Dispersion characteristics for plasma resonances of Maxwellian and Kappa distribution plasmas and their comparisons to the IMAGE/RPI observations, *J. Geophys. Res.*, *110*, A06202, doi:10.1029/2004JA010967.

Xiao, F., Q. Zhou, H. He, H. Zheng, and S. Wang (2007), Electromagnetic ion cyclotron waves instability threshold condition of suprathermal protons by kappa distribution, *J. Geophys. Res.*, *112*, A07219, doi:10.1029/2006JA012050.

Xiao, F., C. Shen, Y. Wang, H. Zheng, and S. Wang (2008), Energetic electron distributions fitted with a relativistic kappa-type function at geosynchronous orbit, *J. Geophys. Res.*, *113*, A05203, doi:10.1029/2007JA012903.

Xiao, F., L. Chen, Y. He, Z. Su, and H. Zheng (2011), Modeling for precipitation loss of ring current protons by electromagnetic ion cyclotron waves, *J. Atmos. Sol. Terr. Phys.*, *73*, 106–111, doi:10.1016/j.jastp.2010.01.007.

Xiao, F., Q. Zhou, Z. He, and L. Tang (2012), Three-dimensional ray tracing of fast magnetosonic waves, *J. Geophys. Res.*, *117*, A06208, doi:10.1029/2012JA017589.

Xiao, F., Q. Zhou, Z. He, C. Yang, Y. He, and L. Tang (2013), Magnetosonic wave instability by proton ring distributions: Simultaneous data and modeling, *J. Geophys. Res. Space Physics*, *118*, 4053–4058, doi:10.1002/jgra.50401.

Xiao, F., Q. Zhou, Y. He, C. Yang, S. Liu, D. N. Baker, H. E. Spence, G. D. Reeves, H. O. Funsten, and J. B. Blake (2015a), Penetration of magnetosonic waves into the plasmasphere observed by the Van Allen Probes, *Geophys. Res. Lett.*, *42*, 7287–7294, doi:10.1002/2015GL065745.

Xiao, F., C. Yang, Z. Su, Q. Zhou, Z. He, Y. He, D. N. Baker, H. E. Spence, H. O. Funsten, and J. B. Blake (2015b), Wave-driven butterfly distribution of Van Allen belt relativistic electrons, *Nat. Commun.*, *6*, 8590, doi:10.1038/ncomms9590.

Zhang, J.-C., et al. (2014), Excitation of EMIC waves detected by the Van Allen Probes on 28 April 2013, *Geophys. Res. Lett.*, *41*, 4101–4108, doi:10.1002/2014GL060621.

Zhou, Q., et al. (2014), Excitation of nightside magnetosonic waves observed by Van Allen Probes, *J. Geophys. Res. Space Physics*, *119*, 9125–9133, doi:10.1002/2014JA020481.